Key intermediates and Cu active sites for CO2 electroreduction to ethylene and ethanol

nature energy

Article

https://doi.org/10.1038/s41560-024-01633-4

# Key intermediates and Cu active sites for $CO_2$ electroreduction to ethylene and ethanol

Received: 20 April 2023

Accepted: 9 August 2024

Published online: 11 September 2024

Check for updates

Chao Zhan[1,4], Federico Dattila[2,3,4], Clara Rettenmaier[1], Antonia Herzog[1], Matias Herran[1], Timon Wagner[1], Fabian Scholten[1], Arno Bergmann[1], Núria López[2] ✉ & Beatriz Roldan Cuenya[1] ✉

Electrochemical reduction of $CO_2$ ($CO_2$RR) to multi-carbon products is a promising technology to store intermittent renewable electricity into high-added-value chemicals and close the carbon cycle. Its industrial scalability requires electrocatalysts to be highly selective to certain products, such as ethylene or ethanol. However, a substantial knowledge gap prevents the design of tailor-made materials, as the properties ruling the catalyst selectivity remain elusive. Here we combined in situ surface-enhanced Raman spectroscopy and density functional theory on Cu electrocatalysts to unveil the reaction scheme for $CO_2$RR to $C_{2+}$ products. Ethylene generation occurs when *OC–CO(H) dimers form via CO coupling on undercoordinated Cu sites. The ethanol route opens up only in the presence of highly compressed and distorted Cu domains with deep *s*-band states via the crucial intermediate *$OCHCH_2$. By identifying and tracking the critical intermediates and specific active sites, our work provides guidelines to selectively decouple ethylene and ethanol production on rationally designed catalysts.

Electrochemical reduction of $CO_2$ ($CO_2$RR) to chemicals is a promising approach to store intermittent renewable energy as valuable fuels and feedstocks[1,2]. In particular, the synthesis of multi-carbon ($C_{2+}$) products, such as ethylene and ethanol, is highly attractive because of their versatility in the chemical and energy industries[3], and processes involving C–C bond formation are of great relevance from the point of view of fundamental research[2,4].

Copper-based materials are the most selective catalysts for electrochemically reducing $CO_2$ to $C_{2+}$ products[2]. A myriad of studies have focused on understanding the C–C coupling mechanism, and although some consensus has been reached, the dependence of these paths on the particular material history is yet to be confirmed[5,6]. Several coupling pathways have been proposed[7,8], suggesting adsorbed CO (*CO) as the building block of multi-carbon products[5,9,10] via dimerization (OC–CO)[7] or coupling (OC–CHO or OC–COH)[8] steps. Experimentally, *CO has been detected on Cu surfaces using in situ Raman and infrared spectroscopy during $CO_2$RR[6,11,12], and a direct correlation between CO coverage and selectivity towards $C_{2+}$ products exists[13]. Recently, possible C–C coupling intermediates *OCCO or *OCCOH were detected by infrared spectroscopy during the electrochemical reduction of CO (COR)[14,15]. However, while CO coupling has been repeatedly confirmed, observing and tracking potential-dependent CO dimerization and intermediates during the subsequent gradual reduction process towards final products has not yet been achieved.

Among the $CO_2$RR reaction intermediates[7,8], *$OCHCH_2$ is considered the last common precursor in the ethylene and ethanol routes, although experimental confirmation is still missing[2,7]. In fact, glyoxal and glycolaldehyde reduce to acetaldehyde, ethanol and ethylene glycol only on polycrystalline copper[16–18], suggesting an exclusive ethanol-selective route via *$OCHCH_2$. Recently, a methyl carbonyl intermediate, *$OCCH_3$, has been proposed as an alternative intermediate for ethanol and propanol[19,20]. In general, the reaction pathways for ethylene and ethanol formation are defined by logical intuition based on experimental and computational results[7,8,16,21]. However, the lack of

[1]Department of Interface Science, Fritz-Haber Institute of the Max-Planck Society, Berlin, Germany. [2]Institute of Chemical Research of Catalonia (ICIQ-CERCA), The Barcelona Institute of Science and Technology (BIST), Tarragona, Spain. [3]Department of Applied Science and Technology (DISAT), Politecnico di Torino, Turin, Italy. [4]These authors contributed equally: Chao Zhan, Federico Dattila. ✉e-mail: nlopez@iciq.es; roldan@fhi-berlin.mpg.de

https://doi.org/10.1038/s41560-024-01633-4

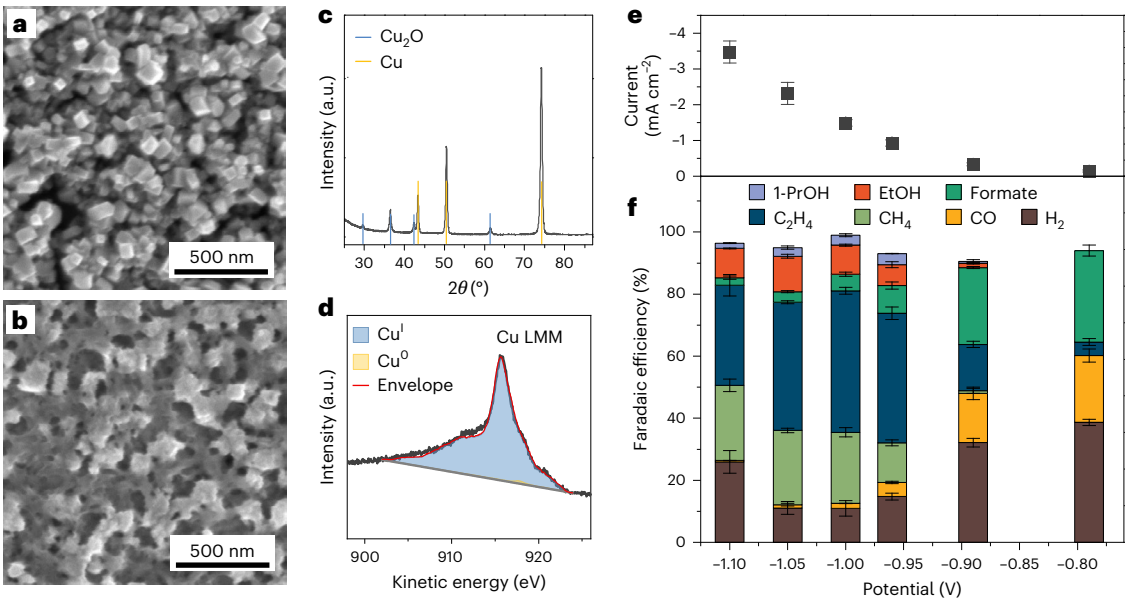


**Fig. 1 | Characterization of the morphology of electrochemically treated Cu foil electrode and its $CO_2$RR performance. a**,**b**, SEM images of an as-prepared (electrochemically treated) Cu foil electrode acquired before (**a**) and after (**b**) $CO_2$RR in $CO_2$-saturated 0.1 M $KHCO_3$ electrolyte at −1.0 $V_{RHE}$ for 1 h. **c**, XRD pattern of the as-prepared Cu foil electrode. **d**, Cu LMM XAES spectrum of the as-prepared Cu foil electrode. **e**, Potential-dependent current density. **f**, Faradaic efficiency of the electrochemically treated Cu foil electrode in $CO_2$-saturated 0.1 M $KHCO_3$ electrolyte for 1 h. The error bars in **e** and **f** correspond to the s.d. of three independent measurements. Data are given as average ± s.d.

robust experimental evidence hinders the rational design of $CO_2$RR electrocatalysts, limiting the overall energy efficiency of the process.

The dynamics of electrocatalysts following charge accumulation, redox chemistry and the presence of adsorbates which can structurally deteriorate the catalyst surface lead to a very complex behaviour[4]. Thus, the generalization of insights gathered through model interfaces in an ultrahigh vacuum (UHV) system needs to be compared with the in situ electrocatalytic solid–liquid interface[22]. So far, a direct link between the local atomic surface structure and the Cu coordination environment on the catalytic process and, in particular, its influence on distinct reaction pathways remains unclear. CO strongly deteriorates the Cu surface and leads to undercoordinated sites[23], which has a significant influence on $CO_2$RR. For example, by comparing various single-crystal surfaces with different surface roughness, we previously showed that undercoordinated Cu sites are required for $C_2$ formation[24]. However, it is important to further close this knowledge gap by unravelling how Cu coordination and local stress under reaction conditions affect the catalytic behaviour and thus the full mechanistic picture. To this end, it is required to overcome the challenging low surface coverages of intermediates due to their short lifetimes as well as disentangle the similarities in the vibrational properties of different C–C coupling intermediates[14].

Here we provide direct spectroscopic evidence of potential-dependent CO dimerization and subsequent reduction intermediates during $CO_2$RR on a Cu surface by combining insights from in situ surface-enhanced Raman spectroscopy (SERS) and density functional theory (DFT)-based vibrational analysis. This allows us to identify crucial Cu sites and surface intermediates for either ethylene or ethanol, leading to the definition of an updated reaction scheme for $CO_2$RR to $C_2$ products.

## Electrode preparation and $CO_2$RR test

The Cu electrodes were prepared by an electrochemical oxidation–reduction process (see Methods for details). Scanning electron microscopy (SEM) images show the formation of cubic structures with high density (Fig. 1a,b and Supplementary Fig. 1). The X-ray diffraction (XRD) pattern confirms the presence of $Cu_2O$ (Fig. 1c). Cu LMM X-ray Auger electron spectroscopy (XAES) data indicate a surface composition of about 94% $Cu^I$ and 6% $Cu^0$ species (Fig. 1d and Supplementary Fig. 2), while further elemental analysis confirmed the absence of other elements, such as Na, Cl and S (Supplementary Fig. 3). After 1 h of $CO_2$RR at −1.0 $V_{RHE}$ (where RHE is reversible hydrogen electrode) in 0.1 M $KHCO_3$, the XRD pattern of $Cu_2O$ almost completely disappeared (Supplementary Fig. 4), and the cubic morphology partially changed (Fig. 1b), consistent with previous reports[13]. In spite of these morphological changes, no unexpected elements (for example, K) were present in post-catalysis X-ray photoelectron spectroscopy (XPS) analysis (Supplementary Fig. 5). Thus, we opted to use this treatment to obtain sufficient enhancement of the Raman signals.

Similar to the oxide-derived Cu (OD-Cu) materials, which are selective for C–C coupling[24–27], the as-prepared Cu electrode with a high electrochemical surface roughness factor (14.6; Supplementary Fig. 6, electropolished Cu foil as a reference) shows high performance towards $C_{2+}$ products and provides the opportunity to detect C–C coupling intermediates[25]. The specific current densities increase up to at least −1.1 V (Fig. 1e), while the Faradaic efficiencies of $CO_2$RR products and $H_2$ vary strongly with the applied potential (Fig. 1f). The Faradaic efficiencies of $C_{2+}$ products show a typical volcano dependence on the applied potential, with a maximum of 65% at about −1.0 $V_{RHE}$. The onset potentials for ethylene and ethanol are about −0.8 $V_{RHE}$ and −0.9 $V_{RHE}$, with these products reaching a maximum value at −1.0 $V_{RHE}$ and −1.05 $V_{RHE}$, respectively.

## Potential-dependent intermediate evolution

To reveal molecular insights into C–C coupling intermediates and their potential dependence, we carried out in situ SERS measurements (Supplementary Fig. 7). Figure 2a shows the in situ Raman spectra acquired at the same position on the electrochemically treated Cu foil electrode as a function of the applied potential in a $CO_2$-saturated 0.1 M $NaClO_4$ electrolyte. A $NaClO_4$ solution leading to a Raman band at ~935 $cm^{-1}$ (Supplementary Figs. 8 and 9) was used to decrease the influence of highly concentrated bicarbonate in the wavenumber

https://doi.org/10.1038/s41560-024-01633-4

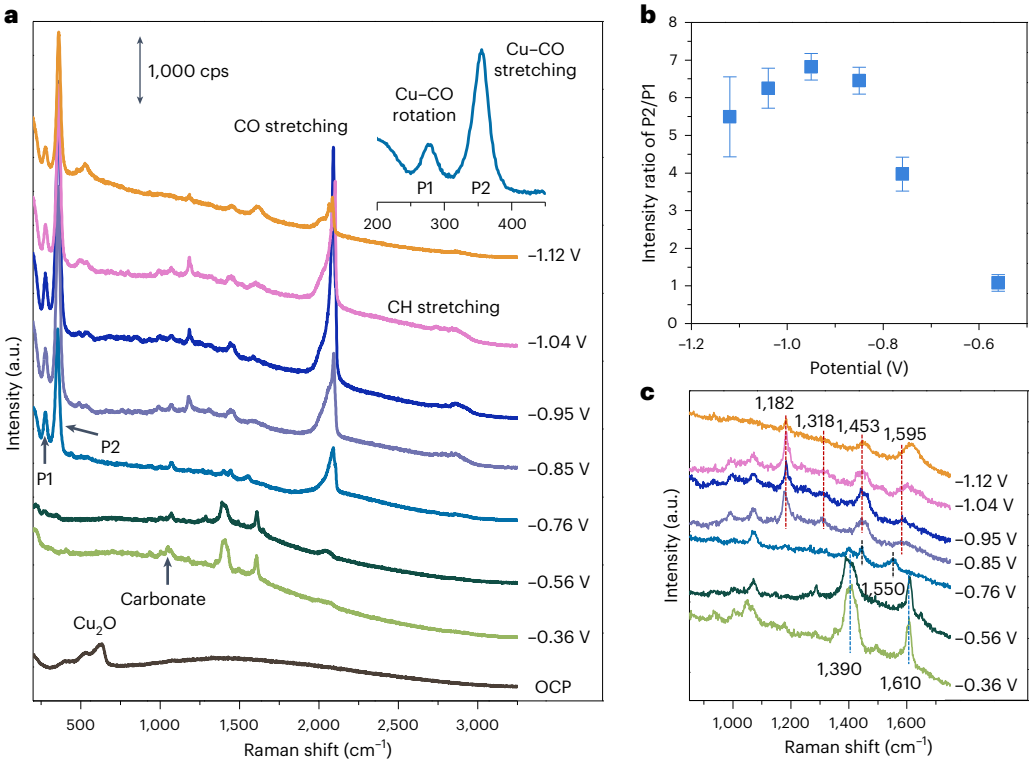


**Fig. 2 | In situ SERS measurement during $CO_2$RR. a**, Raman spectra of an electrochemically treated Cu foil acquired during $CO_2$RR for potentials ranging from the open-circuit potential (OCP) to about −1.1 $V_{RHE}$ in a $CO_2$-saturated 0.1 M $NaClO_4$ electrolyte. cps, counts per second. **b**, Potential-dependent intensity ratio of P2 (Cu–CO stretching, ~360 $cm^{-1}$) to P1 (restricted rotation of adsorbed CO, ~280 $cm^{-1}$). **c**, Zoom-in Raman spectra in the region of 900–1,700 $cm^{-1}$ from about −0.4 $V_{RHE}$ to −1.1 $V_{RHE}$, with relevant peaks highlighted via dashed lines. The error bars in **b** correspond to the s.d. of three independent measurements. Data are given as average ± s.d.

range of 1,000–2,000 $cm^{-1}$ (Supplementary Figs. 10 and 11). We note here that irrespective of the electrolyte anionic species, carbonate and bicarbonate ions will be present due to the $CO_2/H_2O$ equilibrium. Although a lower Faradaic efficiency of $C_{2+}$ products is obtained during $CO_2$RR in $CO_2$-saturated 0.1 M $NaClO_4$ (ref. 28), the onset potentials and potential-dependent trends for ethylene and ethanol formation are similar to those in 0.1 M $KHCO_3$ (Supplementary Fig. 12).

Initially, at open-circuit potential, Raman peaks at 400 $cm^{-1}$, 528 $cm^{-1}$ and 620 $cm^{-1}$ from a $CuO_x$ phase are detected[12,29]. At a potential of −0.36 $V_{RHE}$, the $CuO_x$ is reduced to metallic Cu on the surface, and a small peak is detected at 1,070 $cm^{-1}$, typically assigned to carbonate[13]. Two new peaks at ~1,390 $cm^{-1}$ and ~1,610 $cm^{-1}$ appear, which are attributed to the symmetric and asymmetric stretching vibrations of carboxyl(ate) groups, respectively, based on control experiments in Ar-saturated $NaClO_4$ with 1 mM HCOOH solution (Supplementary Fig. 13) and in Ar-saturated $KHCO_3$ solution (Supplementary Fig. 11).

At −0.56 $V_{RHE}$, peaks of CO adsorbed on Cu are detected, with vibrational features at ~280 $cm^{-1}$, 355–360 $cm^{-1}$ and 1,970–2,110 $cm^{-1}$ corresponding to the restricted rotation of adsorbed CO (P1), Cu–CO stretching (P2) and C–O stretching, respectively. Consistent with our recent finding on the CO coverage-driven C–C coupling mechanism[13], the P2/P1 ratio, a proxy for CO surface coverage on copper, follows a volcano trend with the applied potential (Fig. 2b). At −0.76 $V_{RHE}$, Raman bands at 490–530 $cm^{-1}$ appear, which can be attributed to Cu–O stretching of oxygen or hydroxide species on Cu, or Cu–C stretching[12,29,30]. There are no indications of $Cl^-$ related adsorbates, as the Raman band should appear at ~300 $cm^{-1}$ (refs. 31,32).

More interestingly, the peaks at 1,390 $cm^{-1}$ and 1,610 $cm^{-1}$ disappear with increasing CO surface coverage from −0.56 $V_{RHE}$ to −0.76 $V_{RHE}$, and two new peaks evolve at 1,450 $cm^{-1}$ and 1,550 $cm^{-1}$ (Fig. 2c), which were previously attributed to the *OCCO intermediate[15]. The observation of these peaks agrees well with a CO-coverage-determined C–C coupling during $CO_2$RR[13] and indicates a similar intermediate for C–C coupling during CORR and $CO_2$RR. Concurrently, the Raman peaks of $*HCOO^-$/*HCOOH disappear, which suggests that CO or C–C coupling intermediates may affect the production of formic acid due to competition for surface sites.

At more cathodic potentials, CO coverage further increases, and four new peaks can be detected at 1,182 $cm^{-1}$, 1,318 $cm^{-1}$, 1,453 $cm^{-1}$ and 1,595 $cm^{-1}$ from −0.85 $V_{RHE}$, which show a regular shift with the potential, indicating the existence of new adsorbates. These peaks appeared simultaneously during the time-resolved in situ SERS experiment after a potential switch from −0.36 $V_{RHE}$ to −0.96 $V_{RHE}$ (Supplementary Fig. 14). Concurrently, a broad band in the range of 2,830–2,990 $cm^{-1}$ appeared, which can be attributed to the stretching band of C–H (ref. 12).

## Intermediates responsible for $CO_2$RR to ethylene and ethanol

To confirm the assignment of the vibrational modes detected experimentally, we reverted to DFT (PBE-D2[33]) through the Vienna Ab initio Simulation Package[34,35]. To mimic OD-Cu catalysts, we used two different models. Our first simulation cell consisted of a pristine OD-Cu structure, taken from a Cu(111)/$Cu_2O$(111) epitaxy precursor optimized through ab initio molecular dynamics[36]. Due to the original oxygen-induced reconstruction, Cu surface sites with Cu–Cu coordination numbers varying from 4 to 10 were obtained (Supplementary Figs. 15 and 16). As a reference, a four-layer-thick (100) crystalline supercell (Supplementary Fig. 15) was used, as this facet is often deemed responsible for CO–CO dimerization[10]. Surface atoms in this system were characterized by a Cu–Cu coordination number of 8. To obtain the DFT vibrational frequencies of $CO_2$RR reaction intermediates, we first optimized them on different active sites on the OD-Cu distorted surface and the crystalline

https://doi.org/10.1038/s41560-024-01633-4

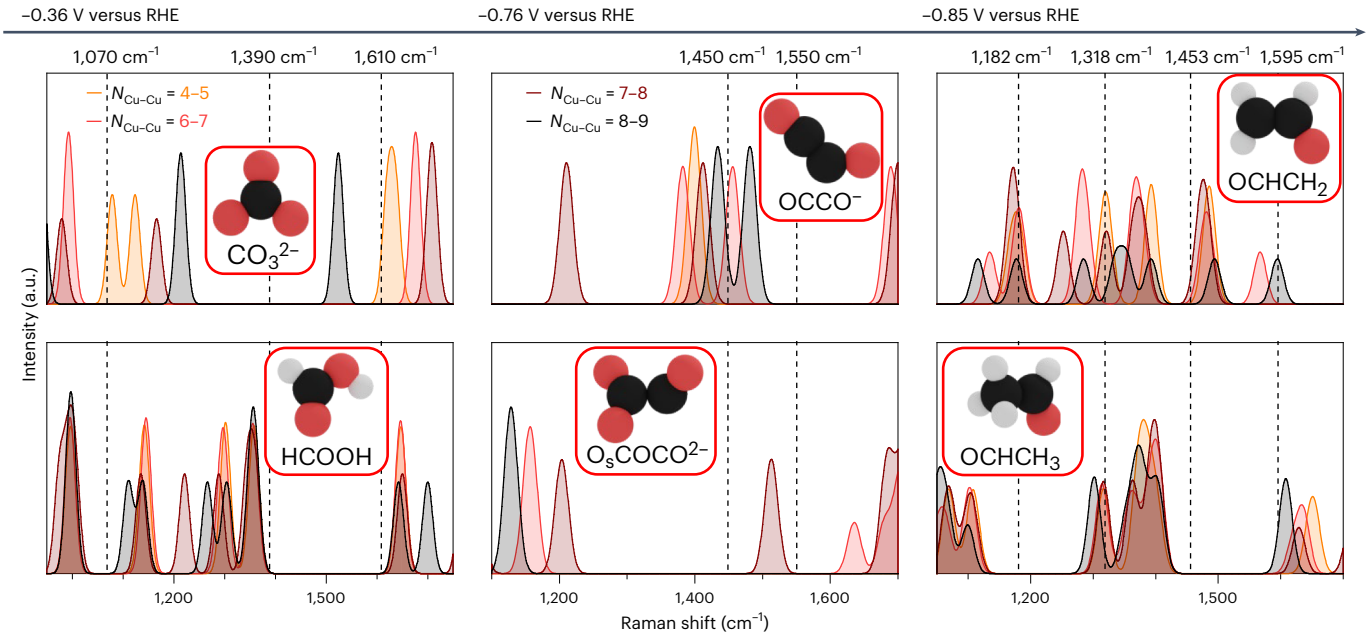


**Fig. 3 | DFT-optimized $CO_2$RR reaction intermediates and their vibrational fingerprints.** DFT vibrational frequencies for $*CO_3^{2-}$, $*COCO^-$, $OCHCH_2$ (top, left to right), *HCOOH, $*O_sCOCO^{2-}$ and $*OCHCH_3$ (bottom, left to right) on adsorption sites with different coordination numbers, increasing from orange to black. Experimental signals at different applied potentials are indicated on top and highlighted in the panels by vertical dashed lines. Raman spectra were achieved by applying a smearing of 10 $cm^{-1}$ on each DFT frequency and overlapping the resulting peaks. Inset: different $CO_2$RR reaction intermediates, with H atoms given in white, O atoms in red and C atoms in black.

Cu(100) and then carried out vibrational analysis on the final configurations. Simulated vibrational frequencies can be visualized through the ioChem-BD database[37] (see the explanatory tutorial in Methods and Supplementary Fig. 17).

In Fig. 3, we show the main reaction intermediates responsible for the vibrational frequencies detected experimentally (Fig. 2a). After the reduction of the Cu oxidic phases, $*CO_3^{2-}$ and $*HCOO^-$/*HCOOH species form (see 1,070 $cm^{-1}$, 1,390 $cm^{-1}$ and 1,610 $cm^{-1}$ signals in Fig. 3; Supplementary Tables 1–3). Consistent with previous reports[14,15], the signals appearing at 1,450 $cm^{-1}$ and 1,550 $cm^{-1}$ from −0.76 $V_{RHE}$ can be attributed to *OCCO(H), with the C=O vibration mode (Fig. 3 and Supplementary Tables 4 and 5). Alternatively, such frequencies can be assigned to an $OCCO^-$ dimer adsorbed on surface oxygen ($O_s$), known as deprotonated glyoxylate $O_sCOCO^{2-}$ (ref. 36), which also shows the 1,070 $cm^{-1}$ band detected at −0.76 $V_{RHE}$ (Supplementary Table 6).

Among other additional possible intermediates (*OCCHO, *OHCCOH, *OCCHOH, *CHO and *CH; Supplementary Tables 7–11), we attribute the 1,182 $cm^{-1}$, 1,318 $cm^{-1}$, 1,453 $cm^{-1}$ and 1,595 $cm^{-1}$ signals detected at −0.85 $V_{RHE}$ and below to the CCO symmetric stretching, CCO antisymmetric stretching, C–C stretching and C–O (or C=C) stretching of $OCHCH_2$ (or $OCHCH_3$) species, respectively (Supplementary Table 7). Although this assignment is based on different independent experiments, we cannot fully rule out that the Raman bands observed might also result from (a set of) very similar adsorbates.

In addition, we carried out $^{13}C$- or D-labelling SERS experiments at −0.95 $V_{RHE}$ (Fig. 4a). $^{13}C/^{12}C$ exchange led to obvious redshifts of the 1,455 $cm^{-1}$ and 1,602 $cm^{-1}$ peaks, in addition to the CO stretching (2,100 $cm^{-1}$), Cu–CO stretching (358 $cm^{-1}$) and CO rotation (275 $cm^{-1}$) bands, proving that these peaks are related to the $CO_2$RR process. Such redshifts were also confirmed by DFT vibrational analysis of $O^{12}CH^{12}CH_2$ and $O^{13}CH^{13}CH_2$ (Fig. 4b and Supplementary Table 12). Water shows a broad O–H bending band at about 1,600 $cm^{-1}$ (refs. 14,15) (Supplementary Table 13), limiting the identification of vibrations from other species in this regime. In agreement with our assignment, the peak at about 1,602 $cm^{-1}$ still appears after the $D_2O/H_2O$ isotope exchange. Besides, the $D_2O/H_2O$ exchange negligibly affected the peaks at about 1,320 $cm^{-1}$ and 1,455 $cm^{-1}$. For the peak at 1,182 $cm^{-1}$, no obvious shift was observed in the D-labelling experiment, while the low intensity in the $^{13}C/^{12}C$ exchange experiment did not allow for a robust determination of the isotope-induced shift.

Since similar C–C coupling intermediates were proposed for CORR[3,38], to validate our observations, we performed in situ SERS during CORR. Our data show similar bands (Supplementary Fig. 18). We further prove the appearance of C–C coupling intermediates by observing analogous signals on a different Cu foil with distinct surface morphology, yet with still good performance towards $C_{2+}$ products (Supplementary Fig. 19).

As ethanol and acetaldehyde are the main $C_2$ products for glyoxal reduction on polycrystalline copper and are proposed to share the same $*OCHCH_2$ intermediate[16–18], we performed in situ Raman experiments of glyoxal and ethanol reduction (Supplementary Figs. 20 and 21). As shown in Fig. 4c, similar bands at about 1,290 $cm^{-1}$, 1,420 $cm^{-1}$ and 1,605 $cm^{-1}$ are observed during glyoxal reduction. We attribute the variations in relative intensities and positions to the substantially different chemical environment in the absence of predominantly co-adsorbed CO, as is the case in $CO_2$RR. The increasing relative intensity of the band at ~1,550 $cm^{-1}$ is probably caused by key intermediates for ethylene glycol formation, which is the dominant product of glyoxal reduction at lower potentials[20]. Instead, these signals were not observed for ethanol reduction (Supplementary Fig. 21). Thus, we reasonably confirmed the detection of a common intermediate along the CO, $CO_2$ and glyoxal reduction route to ethanol, which is $*OCHCH_2$. Overall, the presence of CO molecules on the Cu surface during $CO_2$RR is linked to and probably causes the formation of *CO–CO or *CO–COH at about −0.76 $V_{RHE}$, and then these species further reduce to, for example, $*OCHCH_2$ at −0.85 $V_{RHE}$ and −0.95 $V_{RHE}$.

## Cu active sites selective for $CO_2$RR to ethylene and ethanol

The potential-dependent formation of C–C coupling intermediates explains the selectivity trend towards $C_{2+}$ products observed during $CO_2$RR. In correspondence with an increase in the CO coverage from

https://doi.org/10.1038/s41560-024-01633-4

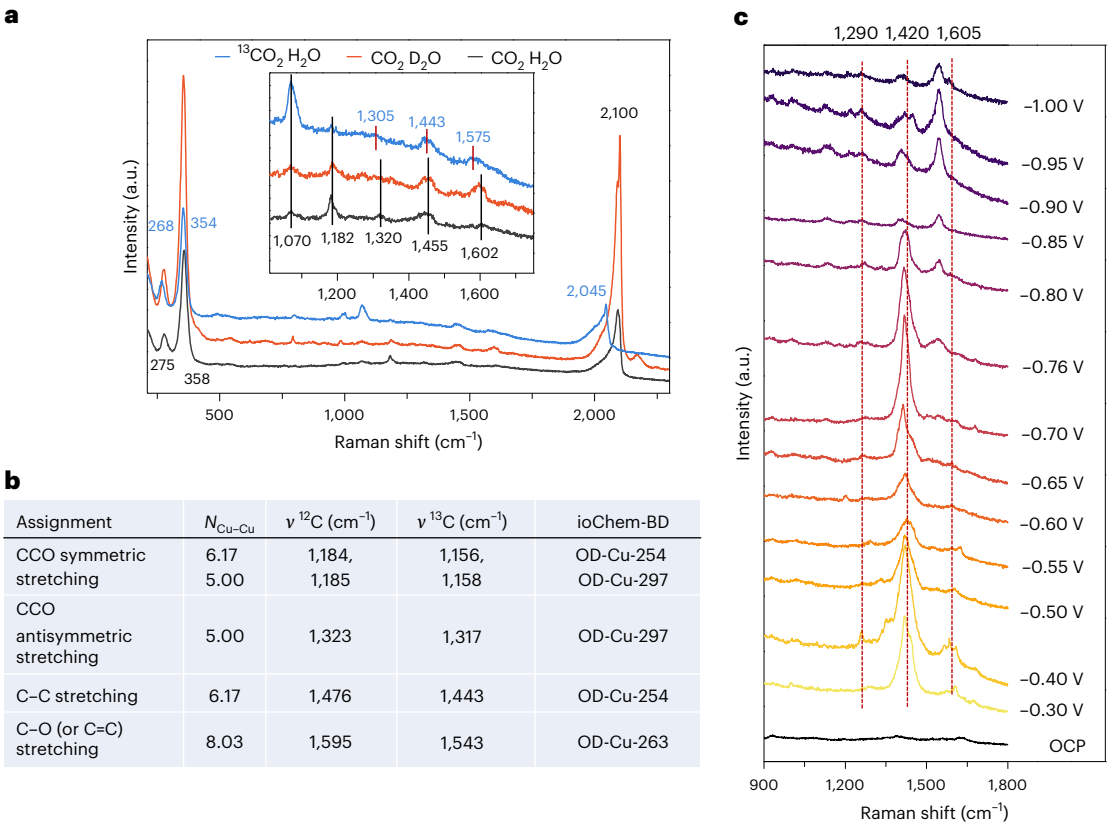


b

| Assignment | $N_{Cu-Cu}$ | $\nu$ $^{12}C$ ($cm^{-1}$) | $\nu$ $^{13}C$ ($cm^{-1}$) | ioChem-BD |
|---|---|---|---|---|
| CCO symmetric stretching | 6.17<br>5.00 | 1,184,<br>1,185 | 1,156,<br>1,158 | OD-Cu-254<br>OD-Cu-297 |
| CCO antisymmetric stretching | 5.00 | 1,323 | 1,317 | OD-Cu-297 |
| C–C stretching | 6.17 | 1,476 | 1,443 | OD-Cu-254 |
| C–O (or C=C) stretching | 8.03 | 1,595 | 1,543 | OD-Cu-263 |

**Fig. 4 | In situ SERS measurement and DFT vibrational analysis with the isotope exchange. a**, Raman spectra of species adsorbed on the electrochemically treated Cu electrode at −0.95 $V_{RHE}$ in $^{13}CO_2$-saturated 0.1 M $NaClO_4$ electrolyte and $CO_2$-saturated 0.1 M $NaClO_4$ $D_2O$ electrolytes. **b**, $OCHCH_2$ vibrational fingerprints on selected active sites determined by DFT simulations for $^{12}C$ and $^{13}C$ (see Methods, ref. 62). **c**, Raman spectra of an electrochemically treated Cu foil acquired in 0.05 M glyoxal for potentials ranging from −0.3 $V_{RHE}$ to about −1.0 $V_{RHE}$ in an Ar-saturated 0.1 M $NaClO_4$ electrolyte.

−0.56 $V_{RHE}$ to −0.76 $V_{RHE}$, the *OCCO intermediate forms on the surface and evolves to ethylene at −0.76 $V_{RHE}$. Instead, the *$OCHCH_x$ key intermediate is detected from −0.85 $V_{RHE}$, the observed onset potential for $CO_2$RR to alcohols. Besides, the ratio of Faradaic efficiencies towards ethanol and ethylene continuously increases with increasingly negative applied potential (Fig. 5a).

To further correlate the catalyst structure, surface intermediates and reaction products, we carried out quasi in situ Cu LMM XAES, in situ SERS, cyclic voltammetry and simulations. The surface of the electrochemically treated Cu foil was fully reduced to metallic Cu after $CO_2$RR at −0.8 $V_{RHE}$ (Fig. 5b). Figure 5c shows the potential-dependent variations of the C–O stretching band of adsorbed CO during $CO_2$RR. The C–O stretching frequency of atop CO on Cu depends on the coordination of the underlying metal atom[39,40]; thus, it can be used as a probe to track the potential-dependent density of different active sites. In principle, the peak shifts to higher wavenumbers for adsorption sites with lower coordination number (although other effects, such as dipole coupling, can interfere)[40], consistent with DFT simulations (Fig. 5d and Supplementary Table 14). Four Gaussian peak functions centred at about 2,035 $cm^{-1}$, 2,075 $cm^{-1}$, 2,090 $cm^{-1}$ and 2,100 $cm^{-1}$ were used to fit the recorded potential-dependent Raman spectra. C–O stretching bands with intermediate frequencies (2,075 $cm^{-1}$ and 2,090 $cm^{-1}$) become the main contribution at −0.76 $V_{RHE}$, from which the *OCCO intermediate is identified and ethylene is produced, in line with the observation of a 2,060 $cm^{-1}$ CO precursor reacting towards C–C coupling as reported in a previous SERS study[6]. At −0.95 $V_{RHE}$, the C–O stretching bands at 2,090 $cm^{-1}$ and 2,100 $cm^{-1}$, assigned to atop CO adsorbed on defect Cu sites, further increase and reach a maximum at −1.04 $V_{RHE}$, coinciding with the detection of the *$OCHCH_x$ key intermediate and ethanol.

The formation of defects on the Cu surface during $CO_2$RR, for instance, adatoms or small Cu clusters with low-coordinated Cu atoms, has been experimentally observed via electrochemical scanning tunnelling microscopy[41]. Moreover, the subsurface incorporation of atomic impurities such as C or O during $CO_2$RR cannot be ruled out, as this could also lead to a defective Cu surface with the modified Raman shifts obtained here. Cyclic voltammetry has been used to compare the defect density on the Cu surface after $CO_2$RR using the charge transferred above +0.3 $V_{RHE}$ (ref. 25). Clearly, $CO_2$RR at −1.0 $V_{RHE}$ induced a higher defect density compared with −0.8 $V_{RHE}$ (Fig. 5e), and the cyclic voltammogram agrees well with that of a restructured/roughened Cu foil upon pulsed electrolysis into the $Cu^{2+}$ regime[25]. These findings are further supported by Pb underpotential deposition experiments[42,43], during which an increased defect site density of $CO_2$RR at −1.0 $V_{RHE}$ was observed (Supplementary Fig. 22). Finally, adsorbed CO linked to a lower C–O stretching band Raman shift becomes preeminent beyond −1.1 $V_{RHE}$, where $CH_4$ production again significantly increases, in line with a previous report[44]. Thus, both in situ SERS and cyclic voltammetry hint at the key role of structural defects in tuning the ethylene/ethanol ratio. These defects are probably formed under reaction conditions and generate distinct surface sites with strong CO binding.

On the basis of these mechanistic insights, we aimed to correlate specific active sites and reaction intermediates with ethylene and ethanol production during $CO_2$RR. Recent experimental studies have highlighted the relevance of defects and polarized Cu sites in enabling $CO_2$RR[25,26,45,46], while flat atomically ordered surfaces mainly yield $H_2$ (ref. 24). Moreover, defective structures and highly disordered Cu(0)/Cu(I,II) interfaces created through pulsed electrolysis conditions were found to significantly enhance ethanol selectivity[25,45,46]. Thus, we initially assessed the role of two structural descriptors to identify defects

https://doi.org/10.1038/s41560-024-01633-4

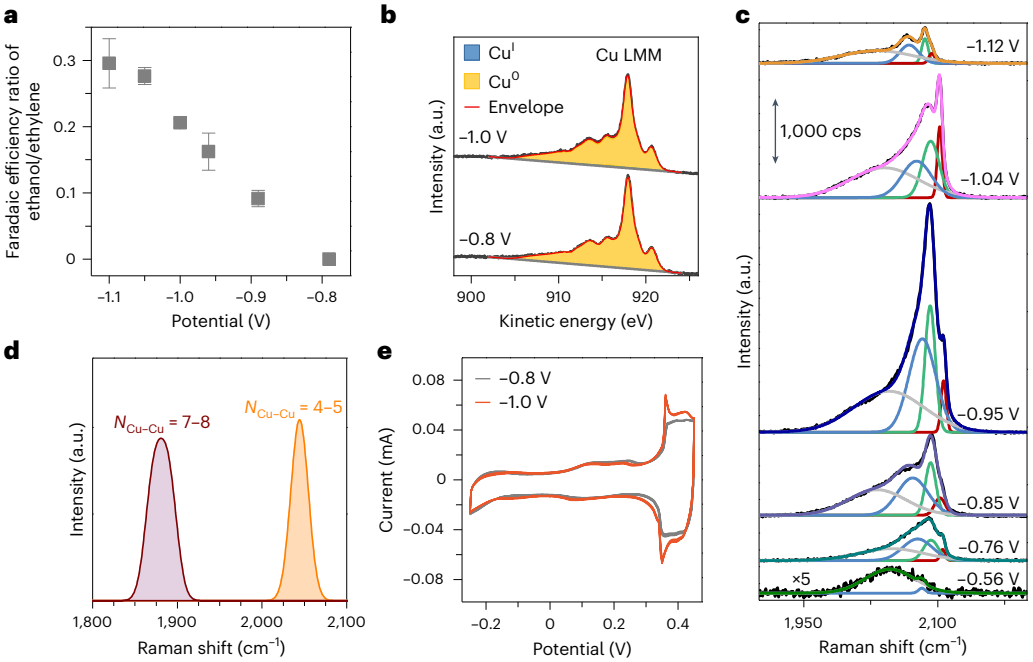


**Fig. 5 | Defect-driven mechanisms for $CO_2RR$ to ethylene and ethanol. a**, Ratio of the Faradaic efficiencies of ethanol and ethylene as a function of the applied potential. **b**, Quasi in situ Cu LMM XAES spectra of electrochemically pre-treated Cu foils after 1 h of $CO_2RR$ at −0.8 $V_{RHE}$ and −1.0 $V_{RHE}$ without air exposure. **c**, Dependence of the C–O stretching band on the applied potential. The Raman spectra are fitted with the sum of 4 Gaussian functions with peaks at about 2,035 $cm^{-1}$ (grey), 2,075 $cm^{-1}$ (blue), 2,090 $cm^{-1}$ (green) and 2,100 $cm^{-1}$ (red). The Raman data in **c** are from the same dataset as those in Fig. 2. **d**, DFT C–O stretching wavenumber as a function of the Cu–Cu coordination number, decreasing from orange ($N_{Cu-Cu}$ = 4–5) to dark brown ($N_{Cu-Cu}$ = 7–8). **e**, Cyclic voltammograms of the electrochemically treated Cu foil after 1 h of $CO_2RR$ at −0.8 $V_{RHE}$ and −1.0 $V_{RHE}$. Cyclic voltammetry was performed in an Ar-saturated 0.1 M NaOH with a scan rate of 50 mV $s^{-1}$. The error bars in **a** correspond to the s.d. of three independent measurements. Data are given as average ± s.d.

among the considered active sites: their coordination number ($N_{Cu-Cu}$; Supplementary Fig. 23) and the relative compressive three-dimensional strain, calculated by dividing the distances between the active site and neighbouring atoms by the Cu–Cu bulk distance ($\Sigma_i(\Delta d_i/d)N_{i,Cu-Cu}^{-1}$ with $i$ ranging from 1 to the number of neighboring atoms, see Supplementary Table 15 and Methods for additional details). Remarkably, the strain does not scale with the coordination number for the distorted sites from the OD-Cu model. Instead, on crystalline domains such as Cu facets and adatoms, both parameters correlate (Supplementary Fig. 23), suggesting a mutual dependence of coordination- and strain-based linear scaling relationships for crystalline sites[47,48].

To sample the reactivity of such surface defects, we estimated the binding energy of atop *CO and $*OCHCH_2$ versus $N_{Cu-Cu}$ and $\Sigma(\Delta d/d)N_{Cu-Cu}^{-1}$. *CO was taken as a $C_{2+}$ selectivity descriptor[10], whereas $*OCHCH_2$ binding strength was used as a descriptor of $OCHCH_2$ stability on the surface. On crystalline domains, *CO binding depends weakly on the strain, in line with results on crystalline surfaces[47], while differences of more than 0.4 eV are observed on highly strained low-coordinated OD-Cu sites (Supplementary Fig. 24 and Supplementary Table 16). Besides, both crystalline and distorted morphologies with coordination number below 8 show strong CO binding (<−0.2 eV).

Localized compressive strain plays a crucial role in stabilizing $*OCHCH_2$ species on distorted sites (red empty data points in Fig. 6a). In fact, $*OCHCH_2$ formation energies increase following the increment of compressive strain, and stronger binding is observed on undercoordinated distorted sites rather than crystalline sites. Such difference between crystalline and distorted sites can be ascribed to their *s*-band states (Supplementary Table 16). Distorted domains present deeper *s*-band states, whereas crystalline sites are characterized by positive *s*-band centres (versus the Fermi energy). The *s*-band equally affects a previously employed descriptor for ethylene/ethanol competition, the *O binding strength[49]. Crystalline sites with a positive *s*-band centre show weak *O binding (black data points in Fig. 6b), whereas distorted sites with a negative *s*-band centre enable strong *O binding, thus promoting the adsorption of intermediates with terminal oxygen along the ethanol route[49]. The *s*-band centre shows a strong correlation with the *d*-band centre (Supplementary Fig. 25 and Supplementary Table 17). Finally, we observe that scaling relationships between the binding energy of adsorbed molecules and strain are heavily affected by the nature of active sites (Supplementary Note 2).

Overall, these insights highlight a clear correlation between active sites and product distribution. Undercoordinated Cu sites enable strong *CO binding, thus sustaining a high CO coverage on the surface, which opens the ethylene pathway via an OCCO(H) intermediate, explaining the evidence of $C_2H_4$ as the only $C_{2+}$ product observed at −0.76 $V_{RHE}$ (Fig. 1f). This scheme explains the typically high $CO_2RR$ selectivity towards $C_2$ of OD-Cu[25], which is due to the abundant undercoordinated sites on these materials[36] (about 74% for $N_{Cu-Cu}$ < 8 on our OD-Cu model; Supplementary Fig. 16). Furthermore, from −0.85 $V_{RHE}$ onwards, undercoordinated distorted sites with high surface strain and deep *s*-band states originate (Fig. 5c,e) and enable the formation of $OCHCH_2$ at the surface (Fig. 6b), detected experimentally through Raman spectroscopy (Figs. 2c and 3) together with the production of ethanol (Fig. 1f).

A careful comparison of ethylene, ethanol and methane Faradaic efficiency versus CO selectivity (taken from Fig. 1f) confirms the existence of key differences between the ethylene and ethanol routes (Fig. 6c). Instead, the similar dependence of ethanol and methane Faradaic efficiency on CO selectivity supports the hypothesis of $CH_x$ as common precursors for the two products, providing additional parallel pathways from CO–$CH_x$ coupling, in line with the recent $CH_3I$/CO reduction study[20]. These undercoordinated distorted sites open the $OCHCH_2$-mediated ethanol route (Fig. 6d).

https://doi.org/10.1038/s41560-024-01633-4

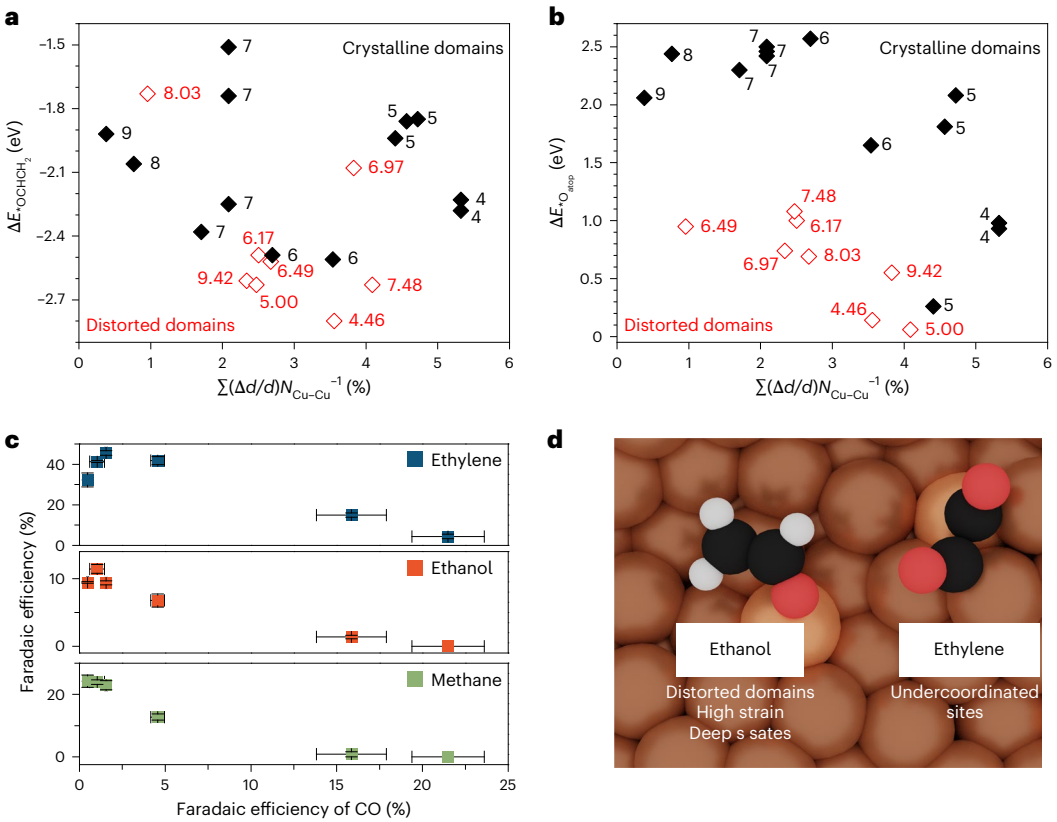


**Fig. 6 | Morphological descriptors for $CO_2R$ to $C_{2+}$ products. a**,**b**, Correlation of *$OCHCH_2$ ($\Delta E_{*OCHCH2}$) (**a**) and *O atop ($\Delta E_{*Oatop}$) binding energies (**b**) versus $\Sigma(\Delta d/d)N_{Cu-Cu}^{-1}$. Cu–Cu coordination numbers are reported as labels. Red data points indicate Cu sites on distorted domains, and black data points represent crystalline domains. **c**, Comparison between ethylene, ethanol and methane Faradaic efficiency versus CO Faradaic efficiency. Data retrieved from Fig. 1f. **d**, Key reaction intermediates and properties of the active sites selective towards ethanol and ethylene, with H atoms given in white, O atoms in red and C atoms in black. The error bars in **c** correspond to the s.d. of three independent measurements. Data are given as average ± s.d.

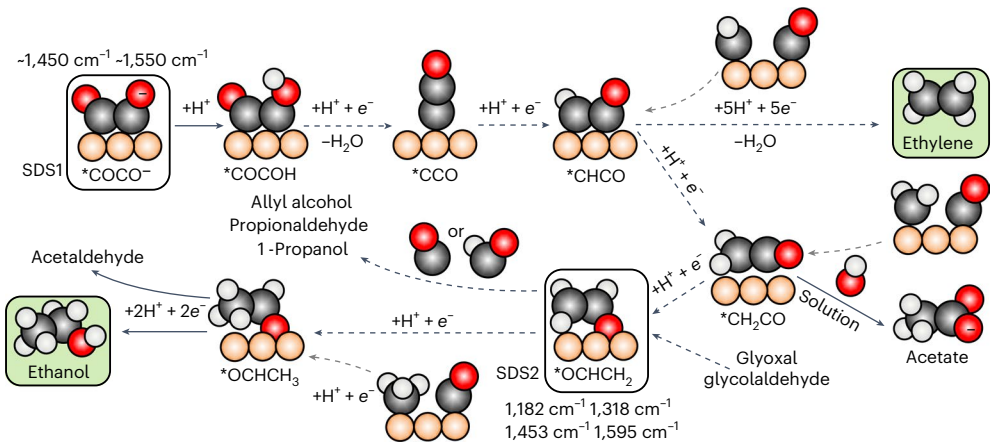


**Fig. 7 | Proposed reaction scheme for $CO_2$ reduction to $C_{2+}$ products.** Proposed reaction scheme, including ethylene and ethanol, was extracted from the present experimental Raman data, our DFT data and additional mechanistic insights reflected in refs. 16,21,51,63. The main $C_{2+}$ products are highlighted in green. Reaction steps confirmed by experimental studies are reported as solid lines, and proposed steps are labelled as dashed lines. Grey arrows indicate potential $CO–CH_x$ coupling routes. H atoms are given in white, O atoms in red and C atoms in black.

## Proposed reaction scheme for $CO_2RR$ to $C_{2+}$ products

The proposed $OCHCH_2$-mediated ethanol pathway suggests an updated reaction scheme for $CO_2RR$ towards $C_{2+}$ products (Fig. 7). Ethylene and ethanol formations are pH-independent on the RHE scale[5]. Thus, according to the state of the art[2,7], CO–CO dimerization, which involves a single electron transfer, is assumed to be the rate-determing step (RDS) towards multi-carbon molecules during $CO_2$ reduction. Such hypothesis has been recently challenged by mechanistic studies of CO reduction[50]; thus, competing RDSs may exist depending on the catalyst morphology. If formed, the CO–CO(H) species is characterized by either a single or double C–C bond[7] (Supplementary Table 18) and acts as a selectivity switch between $C_1$ and $C_{2+}$ products ($C_{2+}$ selectivity-determining step 1, SDS1).

The hypothesis of OCCO(H) as a common $C_{2+}$ precursor for $CO_2$ reduction is reinforced by the strong correlation between ethanol and ethylene Faradaic efficiency on copper ($R^2$ = 0.90, values taken from ref. 51; see Supplementary Fig. 26 and Supplementary Table 19). In line with recent advances[20], additional parallel pathways, such as CO–$CH_x$ coupling (grey arrows, Fig. 7), may also open, yet our DFT simulations disprove any major role of these on distorted sites. In fact, the protonation of $CH_x$ to $CH_{x+1}$ species (and eventually to methane) is always more favourable than the CO–$CH_x$ coupling, apart from the CO–CH case (Supplementary Fig. 27).

Once formed, CO–CO(H) dimers quickly protonate and evolve into an adsorbed ketene *CCO upon the loss of one $H_2O$ molecule, as previously suggested[21,27]. Such ketene then reduces to *CHCO upon proton-coupled electron transfer[7,21], the last common precursor between ethylene and ethanol[49]. *CHCO can then either reduce to *$OCCH_2$ along the acetate/ethanol pathway or undergo reduction to ethylene via five proton-coupled electron transfers and the release of one $H_2O$ molecule[21]. Along the acetate/ethanol route, $OCCH_2$ can desorb and react in solution with $OH^-$ to form acetate[21]. Following the $C_2$ route, when highly strained distorted sites are present, an alternative reaction pathway opens, that is, enabling the reduction of *$OCCH_2$ to *$OCHCH_2$ by strongly binding the terminal oxygen in a monodentate configuration. *$OCHCH_2$ (ref. 7; characterized by a double C–C bond, see Supplementary Table 18) can either reduce to acetaldehyde and ethanol or couple with a CO/COH species to form allyl alcohol and, at later reduction stages, 1-propanol[51] (see the correlation between Faradaic efficiency for both products in Supplementary Fig. 26 and Supplementary Table 19).

Thus, although a methyl carbonyl intermediate ($OCCH_3$) was recently suggested as the ethanol precursor during $CH_3I$ and acetaldehyde/CO reduction[20], we here identify *CHCO reduction to *$OCHCH_2$ as the selectivity switch (selectivity-determing step 2, SDS2) to ethanol, acetaldehyde, 1-propanol and allyl alcohol (Supplementary Note 1 and Supplementary Figs. 28 and 29), as confirmed by the strong correlation between acetaldehyde and ethanol selectivities ($R^2$ = 0.82 (ref. 51); Supplementary Fig. 26 and Supplementary Table 19). Besides, in situ Raman spectroscopy during $CO_2$, CO and glyoxal reduction to ethanol confirms the existence of a shared reaction intermediate, which is reasonably $OCHCH_2$ (Supplementary Fig. 28). The reduction of $OCHCH_2$ to $OCHCH_3$ is thermodynamically sluggish (Supplementary Fig. 30), which might explain the experimental observation of $OCHCH_x$ species, reflecting a significant population on the Cu surface to be detected via SERS on a very rough Cu surface. In fact, a strong *$OCH_2CH_3$ signal was also observed on other ethanol-selective catalysts[52].

## Conclusion

On the basis of in situ SERS and DFT simulations, we identified the crucial active sites and reaction intermediates responsible for ethylene and ethanol formation in $CO_2$RR over a Cu surface. We unveiled that defects in Cu with a low coordination number (<8) enable strong *CO binding, thus sustaining high surface CO coverages and subsequent CO–CO dimerization. These undercoordinated sites are mainly selective to ethylene via the traditional route, *CO–CO or *CO–COH couplings, which are $C_{2+}$ product precursors. However, defects characterized by a highly compressed and distorted coordination environment and deep *s*-band states are instead generated at higher overpotentials and stabilize the adsorption of $OCHCH_2$ via the terminal oxygen, opening an alternative selective route towards ethanol on copper. By combining the potential-dependent evolution of CO adsorption and C–C coupling intermediates, we here describe an updated $CO_2$RR-to-$C_{2+}$ reaction scheme that correlates between active sites, surface intermediates and products. Insights from the identified active sites provide key guidelines to rationally design electrocatalysts to maximize the selectivity of each of these products independently.

## Methods

### Electrode preparations

A commercial polycrystalline copper foil (Advent Research Materials, 99.995%) was used in all experiments. Before each experiment, the copper foil was electropolished at 3 V versus a titanium foil for 3 min in a $H_3PO_4$/$H_2SO_4$ solution consisting of 130 ml $H_3PO_4$ (VWR, 85 wt%), 20 ml $H_2SO_4$ (VWR, 95%) and 60 ml ultrapure water. After that, all working electrodes were rinsed with ultrapure water and placed in the electrochemical cell for the electrochemical oxidation–reduction process. The three-electrode system consisted of the copper foil as the working electrode, a platinum wire as the counter electrode and a leak-free Ag/AgCl reference electrode (LF-1, Alvatek). The copper electrodes were treated at room temperature by cyclic voltammetry in gas-saturated 0.1 M $NaClO_4$ (Aldrich, 99.99%) without the use of halide, at a sweep rate of 10 mV $s^{-1}$ from −1.3 $V_{RHE}$ to +0.9 $V_{RHE}$ for two cycles.

### Characterization of samples

The crystal structure of the catalysts was studied using XRD with a Bruker-AXS D8 Advance in parallel beam configuration equipped with a Cu X-ray tube, a Goebel mirror and equatorial Soller slit (0.3°) as well as an energy-dispersive LynxEye detector. The diffraction pattern was recorded through the grazing incidence mode with an incidence angle of 1° to decrease the bulk contribution of the Cu foil.

The size and morphology of the samples were determined by SEM with a ThermoFisher Apreo microscope and a Hitachi S-4800 system, including a cold field emission gun.

XPS measurements were performed with a commercial hemispherical analyser (Phoibos 150, MCD-9 Detector, SPECS, $E_{pass}$ = 15 eV) and a monochromatic X-ray source (SPECS) with an Al anode ($E_{K\alpha}$ = 1,486.7 eV as X-ray energy) at a power of $P$ = 300 W. All spectra were aligned by fixing the Cu $2p_{3/2}$ of $Cu^0$ and $Cu^+$ to 932.67 eV as a reference.

### In situ Raman experiments

The in situ Raman spectra were obtained using a Renishaw (InVia Reflex) confocal Raman microscope with a 785 nm laser. A water immersion objective with a long working distance (Leica Microsystems, ×63, numerical aperture of 0.9) was chosen to perform the in situ experiments in an electrolyte. The objective with a long working distance was needed to avoid diffusion hindrance during the Raman measurements[13]. During the measurements, the objective was protected from the electrolyte by a Teflon film (DuPont, film thickness of 0.013 mm). The laser power was about 0.36 mW. The acquisition time was 10 s for the steady-state experiments at different potentials. The spot size of the focused laser beam was about 2 µm in diameter. The electrochemical measurements were performed in a home-built spectro-electrochemical cell made of Teflon and controlled by a Biologic SP-240 potentiostat. The cell was equipped with a reference electrode (leak-free Ag/AgCl, Alvatek), a counter electrode (Pt ring) and a Cu foil working electrode. Typically, a 15 ml $CO_2$-saturated 0.1 M $NaClO_4$ solution was used as the electrolyte, and $CO_2$ was continuously injected into the solution during the experiment. Ar-saturated 0.1 M $KHCO_3$ and Ar-saturated 0.1 M $NaClO_4$ were used in the experiments as well. For the steady-state experiment, each potential was applied for at least 10 min before collecting the spectra to ensure steady-state conditions at the surface of the catalyst.

### $CO_2$RR testing

Electrocatalytic measurements were performed with a Biologic SP-240 potentiostat in an H-type cell equipped with an anion exchange membrane (Selemion AMV, AGC). The three-electrode system consisted of the Cu foil as the working electrode, a platinum gauze (MaTecK, 3,600 mesh $cm^{-2}$) as the counter electrode and a leak-free Ag/AgCl reference electrode (LF-1, Alvatek). A $CO_2$-saturated 0.1 M $KHCO_3$ aqueous solution, purified from trace metal ion impurities by a cation-exchange resin (Chelex 100 Resin, Bio-Rad), was used as the electrolyte. The

$CO_2$ (99.995%) flow rate was 20 ml $min^{-1}$. For each cathodic potential, the chronoamperometry lasted 3,600 s. All potentials are given versus the RHE scale and were corrected for the *iR* drop. Each presented data point corresponds to an identical freshly prepared sample following this protocol at different potentials. The electrochemical surface roughness factor, estimated from double-layer capacitance measurements, is 14.6, which was measured by cyclic voltammetry in a non-Faradaic potential range from 0.10 $V_{RHE}$ to 0.25 $V_{RHE}$ at scan rates of 20 mV $s^{-1}$, 40 mV $s^{-1}$, 60 mV $s^{-1}$, 80 mV $s^{-1}$ and 100 mV $s^{-1}$ in a $CO_2$-saturated 0.1 M $KHCO_3$ solution after 1 h of electrochemical reaction.

Gas products were detected and quantified every 15 min by online gas chromatography (Agilent 7890B), equipped with a thermal conductivity detector and a flame ionization detector. Liquid products were analysed after each measurement with a high-performance liquid chromatograph (Shimadzu Prominence), equipped with a NUCLEOGEL SUGAR 810 column and a refractive index detector, and a liquid gas chromatograph (Shimadzu 2010 Plus), equipped with a fused silica capillary column and a flame ionization detector[13].

All catalytic results in this study are shown in terms of Faradaic efficiency. The Faradaic efficiency of the gas product *x* was calculated using equation (1):

$$\mathrm{FE} = \frac{\dot{V} \times C_x \times z_x \times \mathrm{F}}{A \times V_\mathrm{M} \times j_\mathrm{total}} \times 100\%, \quad (1)$$

and for the liquid product *x* was calculated using equation (2):

$$\mathrm{FE} = \frac{V \times \Delta C_x \times z_x \times \mathrm{F}}{\Delta Q} \times 100\%. \quad (2)$$

Here FE is the Faradaic efficiency of product *x*, $\dot{V}$ is the $CO_2$ gas flow rate (l $s^{-1}$), $C_x$ is the volume fraction of the product *x* detected by gas chromatography, $z_x$ is the number of electrons transferred for reduction to product *x*, *F* is the Faradaic constant (C $mol^{-1}$), *A* is the geometric area of the electrode ($cm^{-2}$), $V_M$ is the molar volume (22.4 l $mol^{-1}$), $j_{total}$ is the total current density during $CO_2$ bulk electrolysis (A $cm^{-2}$), $\Delta C_x$ is the final concentration of product detected by high-performance liquid chromatography and liquid gas chromatography (mol $l^{-1}$), $\Delta Q$ is the total charge transferred during electrolysis at constant potential or current (C), and *V* is the volume of the electrolyte (l).

### Quasi in situ XPS

Quasi in situ XPS experiments were performed to avoid exposure of the sample to air after the electrochemical treatment. In this set-up, an electrochemical cell is directly attached to the UHV system where the XPS chamber is located to allow the sample transfer without air exposure. The electrochemical measurements were carried out using a potentiostat (Autolab PGSTAT 302N) and a $CO_2$-saturated 0.1 M $KHCO_3$ electrolyte. After the electrochemical treatment, the samples were rinsed with Ar-saturated $H_2O$ and subsequently transferred under an Ar atmosphere into the load-lock of the UHV system.

### DFT details

The DFT calculations were performed using the Vienna Ab initio Simulation Package[34,35], with the Perdew-Burke-Ernzerhof (PBE) density functional[33]. We included dispersion according to the DFT-D2 method[53,54], with the re-parametrization of $C_6$ coefficients for metals performed by our group[55]. To account for solvent stabilization of intermediate formation energy, we employed the VASPsol code[56,57]. Inner electrons were represented by projector augmented wave (PAW) pseudopotentials[58,59], whereas the monoelectronic states for the valence electrons were expanded as plane waves with a kinetic energy cut-off of 450 eV.

We modelled the OD-Cu catalyst investigated experimentally by considering a Cu(111)/$Cu_2O$(111) epitaxy with surface reconstruction induced through ab initio molecular dynamics for 1 + 10 ps (3 fs time step)[36], and a 4-layer thick crystalline Cu(100). For the Cu(100), the two uppermost layers were fully relaxed and the rest fixed to the bulk distances. The Brillouin zone was sampled by a Γ-centred *k*-points mesh from the Monkhorst–Pack method[60], with a reciprocal grid size smaller than 0.03 $Å^{-1}$. The vacuum between the slabs was larger than 12 Å. The adsorbates were placed only on one side of the slab, thus requiring a dipole correction to remove spurious contributions arising from the asymmetric configuration[61]. Formation energies for the selected intermediates were obtained assuming $CO_2$(g), $H_2$(g), $H_2O$(g) and clean surfaces as energy references.

### Cu–Cu coordination number

Two Cu atoms are coordinated if their distance falls below a certain threshold. Since bulk Cu (face-centred cubic) and $Cu_2O$ show Cu–Cu bond distances of 2.57 Å and 3.05 Å, respectively, we assigned a coordination number $N_{Cu-Cu}$ for metallic Cu between 0.0 ($d_{Cu-Cu}$ = 3.05 Å) and 1.0 ($d_{Cu-Cu}$ = 2.57 Å) following a decay controlled by the error function (erf)[36], as shown in equations (3) and (4). In equation (3), $N_{Cu-Cu}$ is the Cu–Cu coordination number (dimensionless), and $d_{Cu-Cu}$ is the Cu–Cu distance (Å). In equation (4), *t* (dimensionless) is the variable of integration, and 0 and *z* represent the integration limits:

$$N_{\mathrm{Cu-Cu}} = \frac{1}{2} - \frac{1}{2}\mathrm{erf}\left(\frac{d_{\mathrm{Cu-Cu}} - 2.57\text{Å}}{0.1\text{Å}}\right) \quad (3)$$

$$\mathrm{erf}(z) = \frac{2}{\sqrt{\pi}}\int_0^z \exp\left(-t^2\right)\mathrm{d}t \quad (4)$$

### Three-dimensional localized strain

Localized three-dimensional strain for a given Cu active site *j* was estimated by assessing the local deformation of Cu–Cu distances versus the bulk value ($d_{Cu-Cu}$(bulk) = 2.57 Å; Supplementary Table 15) for a given atom *i* within the coordination shell of species *j*, as shown in equation (5). Then, such deformations were summed among all the neighbouring Cu atoms and normalized by the Cu–Cu coordination number ($N_{Cu-Cu}$) of the active site *j*, as shown in equation (6). Distances are given in Å, coordination numbers are dimensionless, and three-dimensional strain is reported as a percentage of deformation. Negative values of strain indicate expansion, whereas positive values characterize contraction:

$$\text{3D strain}(j,i) = \frac{d_{\mathrm{Cu-Cu}}(\text{bulk}) - d_{\mathrm{Cu-Cu}}(j,i)}{d_{\mathrm{Cu-Cu}}(\text{bulk})} \times 100 \quad (5)$$

$$\Sigma(\Delta d/d)N_{\mathrm{Cu-Cu}}^{-1}(j) = \sum_{i=1}^{N_{\mathrm{Cu-Cu}}} \frac{\text{3D strain}(j,i)}{N_{\mathrm{Cu-Cu}}^{-1}(j)} \quad (6)$$

### Visualization of vibrational fingerprints

To visualize vibrational frequencies of a given reaction intermediate in ioChem-BD[37], it is necessary to follow the next steps, summarized in Supplementary Fig. 17.

(1) Access ref. 62 and click on the 'frequencies' collection (top left)
(2) Select the desired item to visualize by clicking on the title 'frq-X'
(3) Once a new tab opens, click on 'Actions → View data' (top right)
(4) Once a new tab opens, scroll down to 'vibrational frequencies' and click on it
(5) Click on 'Load vibrations'
(6) Rotate the point of view by pressing the left button of the mouse and select the desired frequency

## Data availability

Regarding the experimental datasets, the data are available in the main text, in the Supplementary Information file or as Source Data files for Figs. 1e,f, 2b, 5a, 6c and Supplementary Fig. 12. Additional data are available from the corresponding authors upon reasonable request. The DFT datasets generated during the current study are available in the ioChem-BD database[37] at https://doi.org/10.19061/iochem-bd-1-251 (ref. 62).

## References


1. Nitopi, S. et al. Progress and perspectives of electrochemical $CO_2$ reduction on copper in aqueous electrolyte. *Chem. Rev.* **119**, 7610–7672 (2019).
2. Birdja, Y. Y. et al. Advances and challenges in understanding the electrocatalytic conversion of carbon dioxide to fuels. *Nat. Energy* **4**, 732–745 (2019).
3. De Luna, P. et al. What would it take for renewably powered electrosynthesis to displace petrochemical processes? *Science* **364**, eaav3506 (2019).
4. Gao, D., Arán-Ais, R. M., Jeon, H. S. & Roldan Cuenya, B. Rational catalyst and electrolyte design for $CO_2$ electroreduction towards multicarbon products. *Nat. Catal.* **2**, 198–210 (2019).
5. Hori, Y., Takahashi, R., Yoshinami, Y. & Murata, A. Electrochemical reduction of CO at a copper electrode. *J. Phys. Chem. B* **101**, 7075–7081 (1997).
6. An, H. et al. Sub-second time-resolved surface enhanced Raman spectroscopy reveals dynamic CO intermediates during electrochemical $CO_2$ reduction on copper. *Angew. Chem. Int. Ed.* **60**, 16576–16584 (2021).
7. Kortlever, R., Shen, J., Schouten, K. J. P., Calle-Vallejo, F. & Koper, M. T. M. Catalysts and reaction pathways for the electrochemical reduction of carbon dioxide. *J. Phys. Chem. Lett.* **6**, 4073–4082 (2015).
8. Garza, A. J., Bell, A. T. & Head-Gordon, M. Mechanism of $CO_2$ reduction at copper surfaces: pathways to $C_2$ products. *ACS Catal.* **8**, 1490–1499 (2018).
9. Hori, Y., Murata, A. & Yoshinami, Y. Adsorption of CO, intermediately formed in electrochemical reduction of $CO_2$, at a copper electrode. *J. Chem. Soc. Faraday Trans.* **87**, 125–128 (1991).
10. Bagger, A., Ju, W., Varela, A. S., Strasser, P. & Rossmeisl, J. Electrochemical $CO_2$ reduction: a classification problem. *Chem. Phys. Chem.* **18**, 3266–3273 (2017).
11. Hori, Y., Koga, O., Yamazaki, H. & Matsuo, T. Infrared spectroscopy of adsorbed CO and intermediate species in electrochemical reduction of $CO_2$ to hydrocarbons on a Cu electrode. *Electrochim. Acta* **40**, 2617–2622 (1995).
12. Moradzaman, M. & Mul, G. In situ Raman study of potential-dependent surface adsorbed carbonate, CO, OH, and C species on Cu electrodes during electrochemical reduction of $CO_2$. *ChemElectroChem* **8**, 1478–1485 (2021).
13. Zhan, C. et al. Revealing the CO coverage-driven C–C coupling mechanism for electrochemical $CO_2$ reduction on $Cu_2O$ nanocubes via operando Raman spectroscopy. *ACS Catal.* **11**, 7694–7701 (2021).
14. Pérez-Gallent, E., Figueiredo, M. C., Calle-Vallejo, F. & Koper, M. T. M. Spectroscopic observation of a hydrogenated CO dimer intermediate during CO reduction on Cu(100) electrodes. *Angew. Chem. Int. Ed.* **56**, 3621–3624 (2017).
15. Kim, Y. et al. Time-resolved observation of C–C coupling intermediates on Cu electrodes for selective electrochemical $CO_2$ reduction. *Energy Environ. Sci.* **13**, 4301 (2020).
16. Schouten, K. J. P., van der Ham, C. J. M., Qin, Z. & Koper, M. T. M. A new mechanism for the selectivity to $C_1$ and $C_2$ species in the electrochemical reduction of carbon dioxide on copper electrodes. *Chem. Sci.* **2**, 1902 (2011).
17. Reichert, A. M., Piqué, O., Parada, W. A., Katsounaros, I. & Calle-Vallejo, F. Mechanistic insight into electrocatalytic glyoxal reduction on copper and its relation to $CO_2$ reduction. *Chem. Sci.* **13**, 11205–11214 (2022).
18. Delmo, E. P. et al. The role of glyoxal as an intermediate in the electrochemical $CO_2$ reduction reaction on copper. *J. Phys. Chem. C* **127**, 4496–4510 (2023).
19. da Silva, A. H. M., Lenne, Q., Vos, R. E. & Koper, M. T. M. Competition of CO and acetaldehyde adsorption and reduction on copper electrodes and its impact on n-propanol formation. *ACS Catal.* **13**, 4339–4347 (2023).
20. Li, J. et al. Intercepting elusive intermediates in Cu-mediated CO electrochemical reduction with alkyl species. *J. Am. Chem. Soc.* **144**, 20495–20506 (2022).
21. Heenen, H. H. et al. Mechanism for acetate formation in electrochemical $CO_{(2)}$ reduction on Cu: selectivity with potential, pH, and nanostructuring Hendrik. *Energy Environ. Sci.* **15**, 3978–3990 (2022).
22. Handoko, A. D., Wei, F., Jenndy, Yeo, B. S. & Seh, Z. W. Understanding heterogeneous electrocatalytic carbon dioxide reduction through operando techniques. *Nat. Catal.* **1**, 922–934 (2018).
23. Auer, A. et al. Self-activation of copper electrodes during CO electro-oxidation in alkaline electrolyte. *Nat. Catal.* **3**, 797–803 (2020).
24. Scholten, F., Nguyen, K.-L. C., Bruce, J. P., Heyde, M. & Roldan Cuenya, B. Identifying structure-selectivity correlations in the electrochemical reduction of $CO_2$: comparison of well-ordered atomically-clean and chemically-etched Cu single crystal surfaces. *Angew. Chem. Int. Ed.* **60**, 19169–19175 (2021).
25. Arán-Ais, R. M., Scholten, F., Kunze, S., Rizo, R. & Roldan Cuenya, B. The role of in situ generated morphological motifs and Cu(I) species in $C_{2+}$ product selectivity during $CO_2$ pulsed electroreduction. *Nat. Energy* **5**, 317–325 (2020).
26. Liu, G. et al. $CO_2$ reduction on pure Cu produces only $H_2$ after subsurface O is depleted: theory and experiment. *Proc. Natl Acad. Sci. USA* **118**, e2012649118 (2021).
27. Li, C. W., Ciston, J. & Kanan, M. W. Electroreduction of carbon monoxide to liquid fuel on oxide-derived nanocrystalline copper. *Nature* **508**, 504–507 (2014).
28. Gao, D. et al. Activity and selectivity control in $CO_2$ electroreduction to multicarbon products over $CuO_x$ catalysts via electrolyte design. *ACS Catal.* **8**, 10012–10020 (2018).
29. Ruiter De, J. et al. Probing the dynamics of low-overpotential $CO_2$-to-CO activation on copper electrodes with time-resolved Raman spectroscopy. *J. Am. Chem. Soc.* **144**, 15047–15058 (2022).
30. Zhao, Y. et al. Speciation of Cu surfaces during the electrochemical CO reduction reaction. *J. Am. Chem. Soc.* **142**, 9735–9743 (2020).
31. Brown, G. M. & Hope, G. A. A SERS study of $SO_2$–$4Cl^-$ ion adsorption at a copper electrode in situ. *J. Electroanal. Chem.* **405**, 211–216 (1996).
32. Niaura, G. & Malinauskas, A. Surface-enhanced Raman scattering from chloride on copper electrodes. *Chem. Phys. Lett.* **207**, 455–460 (1993).
33. Perdew, J. P., Burke, K. & Ernzerhof, M. Generalized gradient approximation made simple. *Phys. Rev. Lett.* **77**, 3865–3868 (1996).
34. Kresse, G. & Furthmüller, J. Efficiency of ab-initio total energy calculations for metals and semiconductors using a plane-wave basis set. *Comput. Mater. Sci.* **6**, 15–50 (1996).
35. Kresse, G. & Furthmüller, J. Efficient iterative schemes for ab initio total-energy calculations using a plane-wave basis set. *Phys. Rev. B* **54**, 11169–11186 (1996).

36. Dattila, F., García-Muelas, R. & López, N. Active and selective ensembles in oxide-derived copper catalysts for $CO_2$ reduction. *ACS Energy Lett.* **5**, 3176–3184 (2020).
37. Álvarez-Moreno, M. et al. Managing the computational chemistry big data problem: the ioChem-BD platform. *J. Chem. Inf. Model.* **55**, 95–103 (2015).
38. Ma, W. et al. Electrocatalytic reduction of $CO_2$ and CO to multi-carbon compounds over Cu-based catalysts. *Chem. Soc. Rev.* **50**, 12897–12914 (2021).
39. Hollins, P., Davies, K. J. & Pritchard, J. Infrared spectra of CO chemisorbed on a surface vicinal to Cu(110): the influence of defect sites. *Surf. Sci.* **138**, 75–83 (1984).
40. Gunathunge, C. M. et al. Spectroscopic observation of reversible surface reconstruction of copper electrodes under $CO_2$ reduction. *J. Phys. Chem. C* **121**, 12337–12344 (2017).
41. Amirbeigiarab, R. et al. Atomic-scale surface restructuring of copper electrodes under $CO_2$ electroreduction conditions. *Nat. Catal.* **6**, 837–846 (2023).
42. Yang, Y. et al. Operando studies reveal active Cu nanograins for $CO_2$ electroreduction. *Nature* **614**, 262–269 (2023).
43. Sebastián-Pascual, P. & Escudero-Escribano, M. Surface characterization of copper electrocatalysts by lead under-potential deposition. *J. Electroanal. Chem.* **896**, 115446 (2021).
44. Bai, H. et al. Controllable CO adsorption determines ethylene and methane productions from $CO_2$ electroreduction. *Sci. Bull.* **66**, 62–68 (2021).
45. Jeon, H. S. et al. Selectivity control of Cu nanocrystals in a gas-fed flow cell through $CO_2$ pulsed electroreduction. *J. Am. Chem. Soc.* **143**, 7578–7587 (2021).
46. Timoshenko, J. et al. Steering the structure and selectivity of $CO_2$ electroreduction catalysts by potential pulses. *Nat. Catal.* **5**, 259–267 (2022).
47. Mavrikakis, M., Hammer, B. & Nørskov, J. K. Effect of strain on the reactivity of metal surfaces. *Phys. Rev. Lett.* **81**, 2819–2822 (1998).
48. Calle-Vallejo, F., Martínez, J. I., García-Lastra, J. M., Sautet, P. & Loffreda, D. Fast prediction of adsorption properties for platinum nanocatalysts with generalized coordination numbers. *Angew. Chem. Int. Ed.* **53**, 8316–8319 (2014).
49. Peng, H.-J., Tang, M. T., Halldin Stenlid, J., Liu, X. & Abild-Pedersen, F. Trends in oxygenate/hydrocarbon selectivity for electrochemical $CO_{(2)}$ reduction to $C_2$ products. *Nat. Commun.* **13**, 1399 (2022).
50. Hou, J., Chang, X., Li, J., Xu, B. & Lu, Q. Correlating CO coverage and CO electroreduction on Cu via high-pressure in situ spectroscopic and reactivity investigations. *J. Am. Chem. Soc.* **144**, 22202–22211 (2022).
51. Kuhl, K. P., Cave, E. R., Abram, D. N. & Jaramillo, T. F. New insights into the electrochemical reduction of carbon dioxide on metallic copper surfaces. *Energy Environ. Sci.* **5**, 7050–7059 (2012).
52. Ding, L. et al. Over 70% Faradaic efficiency for $CO_2$ electroreduction to ethanol enabled by potassium dopant-tuned interaction between copper sites and intermediates. *Angew. Chem. Int. Ed.* **61**, e202209268 (2022).
53. Grimme, S. Semiempirical GGA-type density functional constructed with a long-range dispersion correction. *J. Comput. Chem.* **27**, 1787–1799 (2006).
54. Bucko, T. et al. Improved description of the structure of molecular and layered crystals: ab initio DFT calculations with van der Waals corrections. *J. Phys. Chem. A* **114**, 11814–11824 (2010).
55. López, N. et al. State-of-the-art and challenges in theoretical simulations of heterogeneous catalysis at the microscopic level. *Catal. Sci. Technol.* **2**, 2405–2417 (2012).
56. Fishman, M., Zhuang, H. L., Mathew, K., Dirschka, W. & Hennig, R. G. Accuracy of exchange-correlation functionals and effect of solvation on the surface energy of copper. *Phys. Rev. B* **87**, 245402 (2013).
57. Mathew, K., Sundararaman, R., Letchworth-Weaver, K., Arias, T. A. & Hennig, R. G. Implicit solvation model for density-functional study of nanocrystal surfaces and reaction pathways. *J. Chem. Phys.* **140**, 084106 (2014).
58. Blöchl, P. E. Projector augmented-wave method. *Phys. Rev. B* **50**, 17953–17979 (1994).
59. Kresse, G. & Joubert, D. From ultrasoft pseudopotentials to the projector augmented-wave method. *Phys. Rev. B* **59**, 1758–1775 (1999).
60. Monkhorst, H. J. & Pack, J. D. Special points for Brillouin-zone integrations. *Phys. Rev. B* **13**, 5188–5192 (1976).
61. Makov, G. & Payne, M. C. Periodic boundary conditions in ab initio calculations. *Phys. Rev. B* **51**, 4014–4022 (1995).
62. Dattila, F. Raman-C2. *ioChem-BD* https://doi.org/10.19061/iochem-bd-1-251 (2024).
63. Pablo-García, S. et al. Mechanistic routes toward $C_3$ products in copper-catalysed $CO_2$ electroreduction. *Catal. Sci. Technol.* **12**, 409–417 (2022).


## Acknowledgements

C.Z. thanks the Alexander von Humboldt Foundation (AvH) for supporting his work with an AvH postdoctoral research grant. This work was also partially funded by the European Research Council (ERC-725915, OPERANDOCAT), the Deutsche Forschungsgemeinschaft (DFG, German Research Foundation) – project no. 406944504 – SPP 2080, Germany´s Excellence Strategy – EXC 2008 – 390540038 – UniSysCat, and Bundesministerium für Bildung und Forschung (BMBF, CatLab, 03EW0015A). F.D. and N.L. thank the Spanish Ministry of Science and Innovation (PID2021-122516OB-I00, Severo Ochoa CEX2019-000925-S) for their financial support. We also acknowledge the support from the IMPRS Functional Interfaces Physics and Chemistry and BSC-RES for providing generous computational resources.

## Author contributions

C.Z., F.D., A.B., N.L. and B.R.C. co-wrote the paper. B.R.C. and N.L. supervised the study. C.Z. designed the study and performed sample synthesis, characterization, catalytic measurements and the in situ SERS measurements. A.B. performed the XRD experiments. C.R., M.H., T.W. and F.S. performed the XPS experiments. C.R. performed the Pb UPD experiments. A.H. performed the time-dependent in situ SERS measurements. M.H. performed the in situ SERS measurements of glyoxal and ethanol reduction. F.D. carried out the density functional theory simulations. All authors contributed to the discussion and editing of the paper.

## Funding

Open access funding provided by Max Planck Society.

## Competing interests

The authors declare no competing interests.

## Additional information

**Supplementary information** The online version contains supplementary material available at https://doi.org/10.1038/s41560-024-01633-4.

**Correspondence and requests for materials** should be addressed to Núria López or Beatriz Roldan Cuenya.

**Peer review information** *Nature Energy* thanks Ward van der Stam and the other, anonymous, reviewer(s) for their contribution to the peer review of this work.